Haberland, C., Ryberg, T., Riedel, M., Bauer, K. (2023): Bayesian seismic travel-time cross-hole tomography in vertically transversely isotropic media. - Journal of Applied Geophysics, 209, 104917.

https://doi.org/10.1016/j.jappgeo.2022.104917

Bayesian seismic travel-time cross-hole tomography in vertically transversely isotropic media

Christian Haberland[1], Trond Ryberg[1], Marko Riedel[2,3] & Klaus Bauer[1]

1 Helmholtz Centre Potsdam GFZ German Research Centre for Geosciences, Potsdam, Germany

2 University of Helsinki, Helsinki, Finland

3 now at PROCON IT GmbH, Munich, Germany

Abstract

We apply a transdimensional, hierarchical Markov chain Monte Carlo sampling algorithm (McMC) for 2-D cross-hole travel-time tomography in transversely isotropic media with vertical symmetry axis. The McMC approach has several advantages compared to classical inversion approaches: It is a global search, the high number of tested models allows the statistical analysis including the calculation of a reference model as well as uncertainty estimation, no initial models or regularization parameters are needed, the amount of data noise is automatically determined, and the model parametrization is data dependent and self-adjusting. For the forward solution a FD Fast Marching method utilizing second-order Godunov schemes is used. The performance of the approach is first tested on synthetic datasets to evaluate the potential and possible limitation to recover anisotropic models. We have shown that the recovery of models described by 2 anisotropic parameters (Thomsen parameters) and the vertical velocity is possible for observation scenarios with good distribution of sources and receivers. For more realistic observational geometries (i.e. cross-hole experiments), the recovery of the 3 parameters is limited, but still possible for example for the elliptical anisotropic case (ε=δ) or regarding the horizontal velocity. Finally we applied the McMC approach to a well-studied real cross-

hole data set from the MALLIK 2002 research program and compared the results with previous conventional inversions.

Keywords: Markov chain, Monte Carlo, cross-hole, tomography, seismic, anisotropy, transversal isotropy, gas hydrates, Finite Differences

1. Introduction

Since many years Monte Carlo (MC) sampling approaches are successfully applied to solve inverse problems (e.g., Mosegaard & Tarantola, 1995; Mosegaard & Sambridge, 2002). Instead of solving a set of linear equations (e.g., damped least squares matrix inversion), the stochastic approaches sample the solution space in a more or less random way and determine the models best explaining the measured data. The approaches differ (among others) in the way they sample the model space or whether they can escape from local minima. Popular approaches are genetic algorithms (e.g., Goldberg, 1889), simulated annealing (e.g., Kirkpatrick et al., 1983), or Markov chain Monte Carlo sampling (McMC; Metropolis et al., 1953). MC sampling, especially McMC, has several important advantages, i.e., compared to formal inversions (e.g., damped least squares inversion): 1) the model space is thoroughly sampled (it is considered a global search). 2) The resulting suite of well fitting models can be statistically analyzed by calculating e.g. average/reference models, estimates of uncertainties, etc. In formal inversions usually only one best fitting model is calculated. 3) Depending on the specific inversion problem, no linearization of the problem or assumptions on regularization or damping are required. 4) Only minimal prior assumptions are needed, for example no initial models or pre-defined parametrization are required (data-driven inversion). Finally, 5) the methods are well suited to simultaneously search for different (physical) parameters.

Recently, further modifications boosted the geophysical applications of the McMC methods (e.g., Bodin and Sambridge, 2009; Bodin et al., 2012a,b). In the so-called transdimensional McMC inversion, the model parametrization (i.e. the number of model parameters) is automatically adjusted depending on data distribution, quality and quantity (e.g., Bodin et al., 2012b). In the hierarchical McMC inversion the noise of the data, which is often not well known, is automatically estimated by the algorithm (e.g., Bodin et al., 2012a). McMC methods are typically computationally expensive, however, today‘s computer power allows to solve even larger inversion problems with McMC methods.

McMC is now successfully applied to a number of geophysical problems such as surface wave or ambient noise tomography (Shapiro & Ritzwoller, 2002; Galetti et al., 2016), geoacoustic inversion (Dosso et al., 2014), local earthquake location (Gesret et al., 2015; Ryberg & Haberland, 2019), local earthquake tomography (Agostinetti et al., 2015), controlled source refraction seismic tomography (Ryberg & Haberland, 2018), geoelectric sounding (Schott et al., 1999), electromagnetic data (Mandolesi et al., 2018), reflection seismic data (Sen & Biswas, 2017) or gravity (Titus et al., 2017). Further discussion is given for example by Sambridge & Mosegaard (2002).

In this paper we present an implementation of the transdimensional, hierarchical McMC search to derive the anisotropic seismic velocity structure of the subsurface for a cross-hole acquisition geometry, specifically for transversely isotropic media with a vertical symmetry axis (i.e., vertical transverse isotropy – VTI), to benefit from the advantages of this method listed above.

Cross-hole tomography is an imaging method for the subsurface, originally developed for reservoir investigations (Bois et al., 1971, 1972). The method uses well-to-well measurements, which means, that seismic sources situated in one borehole are observed by recorders distributed in the other borehole. Sources and/or receivers at the surface can also be included. If large numbers of sources and receivers with a wide aperture are

available, the volume between the boreholes is well covered with criss-crossing rays which form the basis for the successful tomographic reconstruction of the velocity structure (2-D). For traveltime cross-hole tomography the arrival times of the waves emanating from the sources are determined (manually or automatically) and then inverted, often using damped least squares inversion (Bois et al., 1972, Bregman et al., 1989), algebraic reconstruction techniques (McMechan, 1983, Peterson et al., 1985), genetic algorithms (Bichkar et al., 1998) or MC methods (Mewes et al., 2010). The determination of the traveltimes for the forward calculation is an essential step, and straight rays (McMechan, 1983) or curved rays were used (Bois et al., 1971, McMechan et al., 1987, Bregman et al., 1989). Later, also the inversion for attenuation (Bregman et al., 1989; Fehler & Pearson, 1984) as well as for anisotropy (Chapman & Pratt, 1992; Pratt & Chapman, 1992; Carrion et al., 1992; Williamson et al., 1993; Pratt et al., 1993; Mewes et al., 2010) in the cross-hole scenario have been included. Since a number of years the whole wavefield is used in diffraction tomography (Pratt and Worthington, 1988) and in full waveform tomography (e.g., Pratt, 1990; Reiter & Rodi, 1996, Pratt, 1999).

In cross-hole scenarios it is very important to consider the anisotropic case, since sediments often show a pronounced anisotropy due to sub-horizontal bedding (often termed macroscopic or structural anisotropy), cracks, or lattice preferred orientation (e.g., Crampin et al., 1984; Valcke et al., 2006). This is true for the ultrasonic frequency range used in lab experiments and logging as well as for larger wavelengths usually predominant in field experiments such as reflection seismics or cross-hole measurements). Also in crystalline settings anisotropy is regularly encountered. Not accounting for anisotropic effects can introduce large artifacts in the derived models and wrong (isotropic) velocities. However, accounting for anisotropy means a large number of additional free parameters in the tomographic inversion, and a careful estimation of the resolution of the different parameters is therefore essential. Even in the isotropic case artifacts in the tomographic

105 images can be introduced due to the limited aperture of the typical cross-hole measurements and the predominance of sub-parallel raypaths (e.g., Bregman et al., 1989b). This is why we apply here a McMC search to estimate the velocity structure and the uncertainties of the parameters in the anisotropic cross-hole scenario.

110 **2. Method**

The McMC anisotropic cross-hole tomography has two main components: 1) the actual McMC sampling procedure and 2) the calculation of the forward problem (including the parametrization of the model). We mainly follow the procedure outlined in Ryberg & Haberland (2018), in which we applied a McMC sampling to surface-based refraction type 115 experiments. For this study, we extended the parameter space for the anisotropic conditions and replaced the isotropic forward modeling (following Podvin & Lecomte, 1991) by an anisotropic finite difference (FD) traveltime calculation (Riedel, 2016).

We restrict ourselves to the case of transversely isotropic media with a vertical symmetry axis (VTI) which we – to the first order – expect for sub-horizontally layered sediments. 120 Generally, anisotropic seismic wave propagation is related to the elastic properties of the medium which are described by the stiffness tensor (e.g., Babuska & Cara, 1991). The anisotropy can have different symmetry, and a varying number of coefficients of the stiffness tensor is necessary to describe the anisotropy. In its simplest case, a rotational symmetry around a single symmetry axis, which is also referred to as hexagonal symmetry 125 or transverse isotropy, 5 coefficients are required. For a more convenient usage in geophysical applications, Thomsen (1986) introduced three new dimensionless parameters ε, δ and γ, which – in combination with the isotropic (i.e. parallel to the symmetry axis; 0°) phase velocities v_{p0} and v_{s0} – describe the anisotropic behaviour for the case of rotational symmetry (i.e. transverse isotropy). The parameters can be calculated 130 from the coefficients of the stiffness tensor (see e.g. Thomsen, 1986) and are

characteristic of the respective rock types (or more generally, the seismic medium). For (quasi-) P-waves only Ɛ and δ are relevant.

In particular, ε is defined as (Thomsen, 1986)

$$\epsilon = \frac{v_{p90} - v_{p0}}{v_{p0}}$$

with v_{p90} being the horizontal phase velocity. Hence, ε characterizes the ratio of horizontal to vertical velocity while δ is more influential for steeper dipping raypaths as it describes higher-order azimuthal variations of the qP-wavefronts. Thus, δ is more important for example for the move-out of reflected phases in reflection seismics with near-vertical raypaths. In the special case of elliptical qP-wavefronts (elliptical anisotropy), it holds that $\epsilon = \delta$.

2.1 Model parametrization and forward solution

The model is defined by a set of unstructured points $p_i = (x_i, z_i, v_i, \varepsilon_i, \delta_i)$ with x_i, z_i being the spatial coordinates (i.e., distance and depth) of Voronoi cells, and v_i, ε_i and δ_i representing the vertical P-wave velocity (i.e. parallel to the symmetry axis) and two of the Thomsen parameters (assumed to be constant within a cell), respectively. The number of model points varies between 0<i<=N. For the traveltime calculation we generate a fine regular grid comprising all model points as well as all sources and receivers) by sampling the Voronoi model cells. This means that each point of the regular grid is assigned to the set of values of the nearest model point. In this way three grids are created (see Figure 1). Instead of calculating rays and to derive the associated traveltimes we use these grids in an efficient FD-solution of the Eikonal equation to calculate the first-arrival (qP-wave) traveltimes for all points of the grid for each source.

Our FD solution involves the Fast Marching method using second-order Godunov schemes (Sethian, 1996; Sethian & Popovici, 1999) which was extended for anisotropic media by Riedel (2016). The method uses a so-called pseudo-acoustic approximation

(Alkhalifah, 1998, 2000) which is suitable for P-waves and accurate even for stronger degrees of anisotropy. The finite difference approximations work accurately for VTI symmetry, and the implemented Eikonal schemes seems to be more accurate than anisotropic ray tracing approaches, since they do not require an approximation of the group velocity. However, the anisotropic Godunov methods require considerably larger runtime for the VTI implementations compared to their isotropic counterparts because they suffer significantly from the increased algebraic complexity of the anisotropic formulations. So far, the FD solution has successfully been applied for anisotropic prestack-depth migration. For detailed description of the method see Riedel (2016).

Eventually, the root-mean-square (rms) value of the differences between the measured and calculated traveltime values of a particular model for all source-receiver pairs is estimated which is used in the McMC sampling routine as misfit function.

2.2 Transdimensional, hierarchical McMC method

Instead of using conventional, regularization-based inversion methods, we use a probabilistic (statistical) approach to invert for an anisotropic model. In the search of the model space, randomly created models are tested and their capability to explain the data (or misfit, respectively) is evaluated. The models are accepted or rejected according to certain acceptance criteria. Subsequently, new models are then randomly created by perturbation of the previous model, and the evaluation and acceptance process starts again. After the development of a so-called “chain” (Markov chain) of a large number of tested models, the well-fitting models are explored in a statistical way. The application of the method includes issues of model parametrization, solving the forward problem and calculation of a misfit function, the details of the search procedure and – eventually - the statistical analysis of a larger suite of well-fitting models.

We use the transdimensional and hierarchical version of the McMC method, i.e. we do not fix the model dimension (i.e. model complexity or number of cells) a priori, but let it be determined by the data instead. The hierarchical version attempts to invert for data noise as well, i.e. it automatically partitions the traveltime data into a signal component, which can be explained by the model and a noise component, eventually leading to an auto-regularization of the inversion, with the model complexity (i.e., number of cells) being automatically controlled by the data noise level. Since no prior knowledge of the number of cells, starting models and data noise level is needed, the McMC inversion technique will be almost completely data-driven.

To investigate the model space we employ a hierarchical, transdimensional McMC algorithm with a Metropolis-Hastings sampler (Metropolis et al., 1953), following closely the procedures outlined in Bodin et al. (2012a, b). Starting from a randomly chosen model $\mathbf{m_0}$ which is basically an arbitrary number of randomly distributed Voronoi cells, a new model $\mathbf{m_1}$ is drawn from a proposal distribution which depends on the current model. Data are predicted for the new model $\mathbf{m_1}$ and its misfit is calculated (see above). If the misfit of model $\mathbf{m_1}$ is smaller than the one for model $\mathbf{m_0}$, it will be accepted. If the new model has a higher misfit, the model is rejected with a high probability and a new model is generated (see below), however, there is a non-zero probability that a model with larger misfit is still accepted. This procedure allows for the escape from local minima and makes the McMC method a global search method. The whole sequence is repeated until convergence is reached, so that the density of samples converges to the posterior probability distribution, for details see for instance Bodin et al. (2012a).

To derive a new model $\mathbf{m_1}$, several model perturbations are considered: moving the nucleus of a randomly selected cell, changing the velocity and anisotropic coefficients of a cell, adding/removing a cell and changing the data noise parameters. The amount of the respective perturbations is controlled by the proposal probability distribution. For velocity

and anisotropic coefficient pertubation proposals, as well as noise and cell move parameters, we choose a Gaussian distribution with zero-mean and standard deviation s for the proposal probability.

Successive models along a Markov chain will not be independent, so we thinned the chain by retaining only every 20th sample of the chain. Before convergence is achieved, all models had been excluded from further analysis. During this burn-in phase the data misfit is still large. This phase is followed by a stationary sampling of the model space (small misfits) in which a large set of models, that fit the data well, will be generated. Statistical properties (mean, standard deviation, modes, etc.) of those models will be used to calculate the final anisotropic velocity models.

We started the individual chains with minimum prior knowledge following the idea of a non-informative or Jeffreys prior to avoid any potential dependence of our final model from those assumptions or potentially uncertain prior information. Each chain was started with a model consisting of a random number of cells (drawn from a gaussian distribution with a mean of 50 and standard deviation of 10), each cell a velocity randomly drawn from a gaussian distribution (mean=2.7 km/s, standard deviation of 0.5 km/s) was assigned. Thomson parameters ε and δ were set to 0 (isotropic starting models). To follow the concept of non-informative priors we chose a potentially wide range for velocity (between 0.1 and 5.0 km/s) and Thomson parameters (between -0.5 and 0.5) in each Voronoi cell during the evolution of the Markov chain to allow comprehensive sampling of the model space.

For the evolution of the Markov chains one needs to chose a pertubation or proposal probability distribution with standard deviations (“step size”) for the cell properties (velocity and Thomson parameters) and cell moves (births/death). This choice of these standard deviation controls the speed of chain convergence, by empirical testing we determine optimal values which finally gave acceptance rates between 30 and 40%.

To accelerate the thorough sampling of the model space, we simultaneously started 200 separate Markov chains consisting of 10,000 models each, and combined their output after the burn-in phase (8,000) for further statistical analysis. Finally 20,000 models, all of them fitting the data very well, had been used to derive statistical model properties: the anisotropic velocity distribution, which is the so-called reference model, and the data noise level. Mean values and standard deviation (uncertainty or errors) for velocity and Thomson parameters had been calculated at every grid point of the reference model.

3. Synthetic tests

We firstly tested the implementation of the algorithm for a simple model consisting of a circular anisotropic anomaly superimposed over a homogeneous model. We used 20 sources and receivers with coinciding locations, distributed regularly around the anomaly. We consider this an almost ideal observation geometry. We calculated synthetic traveltimes and added gaussian distributed noise with RMS=0.075 ms. For the forward calculations and inversion we used a 100x100 grid with 1 m spacing. This data set was inverted for v, ε and δ (for parameter definitions see chapter 2) and data noise. Figure 2A and B shows the evolution of the Markov chains, in particular the data misfit and number of Voronoi cells. The input and recovered models are shown in Figure 2C, D, E and F, G, H, respectively. The difference between the recovered and input models (Figure 2 I, J, K) shows that the recovery was successful, with the strongest differences directly at the boundary of the anomaly, an effect we have expected. It is a well-known effect that at sharp velocity boundaries the uncertainty of that velocity is increased which had been described as “loops of uncertainty” (see Galetti et al., 2015). It might be interesting that the recovery of a circular anomaly is still possible with sufficient accuracy when using Voronoi cells, somewhat contradicting the intuition of describing a circular shaped object by a finite number of polygonal Voronoi cells. As illustrated by the good recovery of the circular

anomaly the superposition of a large number of well-fitting models allows for imaging structures and shapes at a much smaller scale than the individual coarse Voronoi models where resolved, a phenomenon called super-resolution. We conducted several synthetic tests with this “ideal” geometry with different values for ε and δ (positive and negative) and found similar good recovery. In addition to the model reconstruction, we could successful recover the level of noise which was added to the synthetic travel times.

In a second test we investigated the capability of the McMC approach of recovering still simple anomalies, but this time, using a more realistic source and receiver distribution taken from a real cross-hole seismic experiment (48 source and 454 receiver positions). Figure 3A, B and C show the synthetic model for v, ε and δ, consisting of isotropic and anisotropic horizontal layers embedded in a homogeneous isotropic background. With the given sources and receivers on opposite sides in the model, the expected ray coverage (for simplicity straight rays) is show in Figure 3D. Compared to the first test (Figure 2) the azimuthal coverage is not significantly exceeding 90°. Again, for this model synthetic traveltimes are calculated, noise was added and a McMC inversion was performed (same values for starting model choice and proposal distributions as in example before). Instead of showing the differences between the recovered and input models (Figure 2), we analyzed the posterior distribution of v, ε and δ at 4 exemplary locations, marked as D, E, F and G in Figure 4. Figure 4 D, E, F and G shows the posterior distribution and the input values (green line). At location F and G the recovery of the properties is in good agreement with the input model. The recovery of the isotropic layer (D) shows a small, but systematic shifted towards apparent weak anisotropy. Also the horizontal velocity is well recovered, however, a significant deviation is observed in the anisotropic layer at location E: there the recovery of the model fails: v is overestimated, δ is significantly underestimated and significant heterogeneity in the middle anisotropic layer (in particular the δ parameter) is introduced. However, the horizontal velocity is quite well recovered.

We think that the failure to unambiguously recover all 3 parameters (i.e., vertical velocity v and 2 Thomsen parameters ε and δ) is related to the limited azimuthal coverage due to the experiment geometry which is mainly given by the distribution of sources and receivers. We suspect that placing sources and/or receivers at the Earth's surface might potentially reduce these imaging limitations. Nevertheless, we would like to emphasize that despite the trade-offs between v, δ and ε, the horizontal velocity is well resolved.

In a next step we further reduced the model complexity by using only 1 instead of 2 independent Thomsen parameters, resulting – together with the vertical velocity - in 3 independent model parameters. In this test we assumed elliptical anisotropy with ε=δ for the same general model as in Figure 3. We analyzed the posterior distribution of v and ε (=δ) at the same locations as in Figure 4. Figure 5 shows the recovered model. In the elliptical case, the recovery of the input model is significantly improved, with only minor deviations of the inverted model from the input one (e.g. Figure 5 C, ε (=δ)). In the elliptical case with the present observational geometry the recovery of v and ε (= δ) seems appropriate to be applied to real observational data.

4. Application to real data

We apply the McMC cross-hole tomography approach to an intensively analyzed dataset from the MALLIK 2002 Production Research Well Program (Takahashi et al., 2005). Within this program, three holes each around 1150 m deep, were drilled through gas-hydrate layers in the Mackenzie delta (Northwest Territories, Canada). Between holes 3L-38 and 4L-38, 85 m apart, cross-hole seismic measurements were performed in a depth range between 800 and 1150 m. As source, a high-power, piezo-ceramic swept frequency source was used, recorded by a hydrophone recording string. After cross-correlation of the raw data with the sweep signal, data were filtered in the frequency-wavenumber domain to reduce the influence of tube waves, and the first arrival times of the P-body waves were

determined (picking). More information on the experiment and the data can be found in Bauer et al. (2005a, b).

For our study we use a decimated data set consisting of 10510 arrival times recorded from 48 sources at 454 receiver positions. We assumed elliptical anisotropy (i.e., v and ε=δ) when inverting the traveltime data. For the forward calculations in the inversion we used a 52x190 grid with 2 m spacing. Figure 6 shows the evolution of the data misfit (RMS) and model complexity which is given by the cell numbers of the models for 200 individual Markov chains. After model number 8000 we assumed that the sampling process was stationary, thus the burn-in phase was reached. From the models beyond that point we constructed a reference model (for v and ε=δ) by locally averaging the parameters in each point in the model (Figure 7A and C) and calculating their uncertainties (Figure 7B and D).

The velocity model is characterized by several layer-like units with increased velocities (Vp up to 3.4 km/s), interlaced with layers of lower velocities (around 2.2 km/s). In the high-velocity layers we observe elevated values for the anisotropy (up to ε=δ=0.2), however, also in the depth range of 1000 to 1050 m which is actually characterized by low seismic velocities, we recovered increased anisotropy. In general, the distribution of the anisotropy (ε=δ) is not as sharp as their expressions in v. The uncertainties estimated from the 1σ of the well-fitting models (see e.g., Figure 7) for v are in the order of up to 0.2 km/s and for ε (=δ) in the range of 0.05. Predominant purple and bluish colors in Figure 7B indicate a relatively evenly distributed small uncertainty and therefore good resolution in most of the model except for a small zone of triangular shape at 1120 – 1160 m depth (greenish colors in Figure 7B indicating increased uncertainties up to 0.5 km/s) probably related to the limited ray coverage. Furthermore, similar to the “loops of uncertainty” (see section 3 and Figure 2 I, J, K, see also Galetti et al., 2015) sub-horizontal bands/strings of greenish color in Figure 7B indicating elevated uncertainties, which could be termed “strings of uncertainty”, suggest relatively sharp boundaries between the different anomalies. The

algorithm needs approximately 60 to 100 model nodes (Voronoi cells) to fit the data well. Running the inversion accounting for VTI media yielded a final RMS value of 0.430 ms, which is significantly smaller compared to the purely isotropic case which yielded a final RMS value of 0.524 ms (see Figure 8). Also, less pronounced coherent patches of larger residuals in the anisotropic case (Figure 8) indicate that anisotropy is needed to explain the data.

5. Discussion and Conclusions

A transdimensional, hierarchical McMC utilizing an anisotropic FD forward simulation has been successfully applied for the inversion of cross-hole seismic traveltime data. The advantage of using a hierarchical, transdimensional McMC approach to invert for anisotropic structures from travel time data relates to the fact that almost no prior assumptions are needed, i.e. starting models, number of cells to be inverted, noise level of the data, etc. Classical inversion techniques typically require such prior information, leading consequentially to a potential dependence of the final model from those assumptions. The McMC technique with its global search capabilities, significantly reduces the risk to “fall” into a local misfit minimum, again overcoming a potential thread of classical inversion approaches. Another advantage of the McMC inversion consists of the recovery not only of the velocity and anisotropic parameters but also their uncertainties.

The VTI-FD forward calculation (Riedel, 2016) proved to be very well suited although the computation time compared to the isotropic FD forward calculation (e.g. Podvin & Lecomte, 1991) is significantly larger.

Our synthetic test with perfect observation geometries showed that the anisotropic parameters v (vertical velocity) and the two Thomsen parameters ε and δ could be very well recovered. The synthetic tests using typical subsurface conditions and cross-hole observation geometries showed limitations to recover all three parameters to describe the

anisotropy. Although the horizontal velocity could be well recovered, there are some trade-offs between the three parameters, and ε, δ and the vertical velocity v could not be unambiguously recovered throughout all parts of the model. We attribute this to the much larger number of free parameters to be inverted for compared to the isotropic case in concert with the limited aperture of the measurements. It seems that the limited aperture hampers capturing of the subtle azimuthal traveltime variations (i.e. the azimuthal anisotropy), and v, ε and δ can hardly be independently resolved. This problem has already been noted e.g. by Williamson et al. (1993) who found a high degree of non-uniqueness and ambiguities in cross-hole inversion scenarios in the case of three free and independent parameters (v, ε and δ) which significantly limits the imaging quality. With a reduced number of parameters the situation seems much more relaxed (less free parameters lead to less ambiguities) and in the elliptically anisotropic case, the parameters could be much better resolved. However, the assumption of elliptical anisotropy (ε=δ), although algebraically simple, is somewhat arbitrary. Thomsen (1986) has pointed out that in real rocks ε and δ are not well-correlated and that the assumption of elliptical anisotropy is physically not well justified. We also ran synthetic test with a fixed δ=0 and found a similarly good recovery as in the case of elliptical anisotropy. However, the way to reduce the number of parameters to be inverted for (ε=δ; δ=const.; etc.) in order to keep the inversion stable should be carefully selected in each individual case. In any case, travel time observations covering a wider azimuth range would be very beneficial and could potentially allow for the inversion for all three parameters v, ε and δ. This could be achieved by an aperture as large as possible as well as sources/receivers distributed along the boreholes, at the surface or at other positions at depth.

The real data inversions from the MALLIK cross-hole experiment showed that significantly better data fits were achieved when accounting for anisotropic conditions instead of assuming isotropic conditions. We take this as strong evidence that our general

anisotropic approach for the inversion of our real data is justified and necessary. The McMC inversion of the real data set revealed very similar results as the inversion with a earlier anisotropic inversion (Bauer et al., 2005a, b; 2008, Figure 9) utilizing the solution by Chapman & Pratt (1992) and Pratt & Chapman (1992). Similar results were also recovered by Giroux & Gloaguen (2012) using a geostatistical approach for elliptical anisotropy. The derived velocity distribution is very similar, also the magnitude of anisotropy is in the same range (ε between 0.1 and 0.2) throughout the model. It has to be noted that Bauer et al. (2005a,b) inverted also for the orientation of the symmetry axis, and a quantitative comparison of the two models is therefore limited. However, their results indicate a subvertical symmetry axis in most parts of the model (see Figure 9 E).

The results show a pronounced sub-horizontal layering of the subsurface. Distinct “strings of uncertainty” (Figure 7B) indicate rather clearly bounded anomalies. The high-velocity anomalies have been related to gas-hydrate bearing layers. They are also consistent with borehole logging. The inversions of the MALLIK data show anisotropy in layers with and without gas-hydrates, and it had been proposed that the anisotropy in the gas-hydrate bearing layers is caused by a partial alignment of clay particles (Pecher et al., 2009). In all sediments, disregarding they are gas-hydrate bearing or not, anisotropy could be expected for instance due to macroscopic layering or preferred mineral orientation (e.g. Babuska & Cara, 1991).

Author contribution: Christian Haberland: Conceptualization, Supervision, Software, Writing – Original Draft. **Trond Ryberg**: Conceptualization, Software, Formal Analysis, Validation, Visualization, Writing – Original Draft. **Marko Riedel**: Software, Writing – Review & Editing. **Klaus Bauer**: Resources, Writing – Review & Editing.

Acknowledgements

The inversion of seismic data was carried out on the high-performance computing cluster at GFZ. Figures were prepared using the Generic Mapping Tool GMT (Wessel and Smith, 1998). MALLIK waveform data (of the real data application) is available through author KB. We thank an anonymous reviewer for helpful comments.

References

Agostinetti, N.P., Giacomuzzi, G. & Malinverno, A. (2015) Local three-dimensional earthquake tomography by transdimensional Monte Carlo sampling, Geophys. J. Int., 201, 1598–1617.

Alkhalifah, T. (1998) Acoustic approximations for processing in transversely isotropic media. Geophysics 63, 623–631.

Alkhalifah, T. (2000) An acoustic wave equation for anisotropic media. Geophysics 65, 1239–1250.

Babuska, V., & Cara, M. (1991) Seismic Anisotropy in the Earth. Kluwer Academic Publishers. Dordrecht, Boston, London.

Bauer, K., Pratt, R. G., Haberland, C., Weber, M. (2008) Neural network analysis of crosshole tomographic images: The seismic signature of gas hydrate bearing sediments in the Mackenzie Delta (NW Canada). - Geophysical Research Letters, 35.

Bauer, K., Haberland, C., Pratt, R. G., Hou, F., Medioli, B., Weber, M. (2005a) Ray-based cross-well tomography for P-wave velocity, anisotropy, and attenuation structure around the JAPEX/JNOC/GSC et al. Mallik 5L-38 gas hydrate production research well. - In: Dallimore, S. R., Collett, T. S.(Eds.), Scientifique Results from Mallik 2002 Gas Hydrate Production Research Well Program, Mackenzie Delta, Northwest Territories, Canada, (GSC Bulletin ; 585), p. 21.

Bauer, K., Pratt, R. G., Weber, M., Ryberg, T., Haberland, C., Shimizu, S. (2005b) The Mallik 2002 cross-well seismic experiment: project design, data acquisition, and modelling studies. - In: Dallimore, S. R., Collett, T. S.(Eds.), Scientific Results from the Mallik 2002 Gas Hydrate Production Research Well Program, Mackenzie Delta, Northwest Territories, Canada, (GSC Bulletin ; 585), Geological Survey of Canada, p. 14.

Bichkar, R.S., Singh, S.K., & Ray, A.K. (1998) Genetic algorithm approach to the detection of subsurface voids in cross-hole seismic tomography. Pattern recognition Letters 19, p. 527 – 536

Bodin, T. (2010) Transdimensional Approaches to Geophysical Inverse Problems. Dissertation, The Australian National University

Bodin, T. & Sambridge, M. (2009) Seismic tomography with the reversible jump algorithm, Geophys. J. Int., 178 (3), 1411–1436.

Bodin, T., Sambridge, M., Rawlinson, N. & Arroucau, P. (2012a) Transdimensional tomography with unknown data noise, Geophys. J. Int., 189 (3), 1536–1556.

Bodin, T., Sambridge, M., Tkalcic, H., Arroucau, P., Gallagher, K. & Rawlinson, N. (2012b) Transdimensional inversion of receiver functions and surface wave dispersion, J. geophys. Res., 117, B02301, doi:10.1029/2011JB008560

Bois, P., La Porte, M., Lavergne, M, & Thomas, G. (1972) Well-to-well seismic measurements. Geophysics, 37 (3), p. 471 – 480

Bois, P., La Porte, M., Lavergne, M, & Thomas, G. (1971) Essai de determination automatique des vitesses sismiques par mesures entre puits. Geophysical Prospecting, 19, p. 42-83.

Bregman, N.D., Chapman, C.H., Bailey, R.C. (1989a) Travel time and amplitude analysis in seismic tomography. J. Geophy. Res. 94 (B6), p. 7577 – 7587

Bregman, N.D., Bailey, R.C., & Chapman, C.H. (1989) Crosshole seismic tomography. Geophysics 54 (2), p. 200 - 2015

Bregman, N.D., Bailey, R.C., & Chapman, C.H. (1989b) Ghosts in tomography: The effects of poor angular coverage in 2-D seismic traveltime inversion. Can. J. Expl. Geophys. 25 (1), p. 7 - 27

Carrion, P., Costa, J., Ferrer Pinheiro, J.E., & Schoenberg, M. (1992) Cross-hole tomography in anisotropic media. Geophysics 57 (9) p. 1194 – 1198.

Chapman., C.H., & Pratt, R.G. (1992) Traveltime tomography in anisotropic media – I. Theory. Geophys. J. Int. 109, p. 1-19

Crampin, S. , Chesnokov, E. M. and Hipkin, R. G. (1984), Seismic anisotropy — the state of the art: II. Geophysical Journal of the Royal Astronomical Society, 76: 1-16. doi:10.1111/j.1365-246X.1984.tb05017.x

Dosso, S.E., Dettmer, J., Steininger, G. and Holland, C.W. (2014) Efficient trans-dimensional Bayesian inversion for geoacoustic profile estimation. Inverse Problems, Volume 30, Number 11.

Fehler, M., & Pearson (1984) Cross-hole seismic surveys: Application for studying subsurface fracture systems at a hot dry rock geothermal site. Geophyics 49 (1), p. 37-45

Galetti, E., Curtis, A., Meles, G.A., Baptie, B. (2015) Uncertainty Loops in Travel-Time Tomography from Nonlinear Wave Physics, Phys. Rev. Lett. 114, doi:10.1103/PhysRevLett.114.148501

Gesret, A., Desassis, N., Noble, M., Romary, T., & Maisons, C. (2015) Propagation of the velocity model uncertainties to the seismic event location. GJI 200, p. 52 – 66; doi: 10.1093/gji/ggu374

Giroux, B., & Gloaguen, E. (2012) Geostatistical traveltime tomography in elliptically anisotropic media. Geophysical Prospecting 60, p. 1133 – 1149

Goldberg, D. E. (1989) Genetic algorithms in search, optimization, and machine learning, Addison Wesley, Boston

Kirkpatrick, S.; Gelatt Jr, C. D.; Vecchi, M. P. (1983). "Optimization by Simulated Annealing". Science. **220** (4598): 671–680.

Mandolesi, E., Ogaya, X., Campany, J., Agostinetti, N. P. (2018) A reversible-jump Markov chain Monte Carlo algorithm for 1D inversion of magnetotelluric data. Computers & Geosciences 113, p. 94-105, doi: 10.1016/j.cageo.2018.01.011.

McMechan, G.A. (1983) Seismic tomography in boreholes. Geophys. J. R. Soc. 74, p. 601 – 612

McMechan, G.A., Harris, J.M., & Anderson, L.M. (1987) Cross-hole tomography for strongly variable media with applications to scale model data. BSSA 77 (6), p. 1945 – 1960.

Metropolis, N., Rosenbluth, A., Rosenbluth, M., Teller, A. und Teller, E. (1953) Equation of State Calculations by Fast Computing Machines. In: Journal of Chemical Physics 21, p. 1087–1092, doi:10.1063/1.1699114.

Mewes, A., Kulessa, B., McKinley, J.D., & Binley, A.M. (2010) Anisotropic seismic inversion using a multigrid Monte Carlo approach. Geophy. J. Int. 183, p. 267 – 276

Mosegaard, K. & Sambridge, M. (2002) Monte Carlo analysis of inverse problems, Inverse Probl., 18 (3), R29–R54.

Mosegaard, K. & Tarantola, A. (1995) Monte Carlo sampling of solutions to inverse problems, J. geophys. Res., 100 (B7), 12 431–12 447

Nath, A.K., Chakraborty, S., Sing, S.K., & Ganguly, N. (1999) Velocity inversion in cross-hole seismic tomgraphy by counter propagatoon neural network, genetic algorithm and evolutionary programming techniques. Geophys J. Int. 138, p. 108 – 124

Pecher, I. A., Holbrook, W. S., Sen, M. K., Lizarralde, D., Wood, W. T., Hutchinson, D. R., Dillon, W. P., Hoskins, H., and Stephen, R. A. (2003), Seismic anisotropy in gas-hydrate- and gas-bearing sediments on the Blake Ridge, from a walkaway vertical seismic profile, Geophys. Res. Lett., 30, 1733, doi:10.1029/2003GL017477, 14.

Peterson, J.E., Paulsson, B.N.P., McEvilly, Th.V. (1985) Applications of algebraic reconstruction techniques in crosshole seismic data. Geophysics 50 (10), p. 1566 – 1580P.

Podvin, L. Lecomte (1991) Finite difference computation of traveltimes in very contrasted velocity models. A massively parallel approach and its associated tools. Geophys. J. Int., 105, pp. 271-284

Pratt, R.G. & Chapman., C.H. (1992) Traveltime tomography in anisotropic media – II. Application. Geophys. J. Int. 109, p. 20-37

Pratt, R.G., McGaughey, & Chapman, C.H. (1993) Anisotropic velocity tomography: A case study in a near-surface rock mass. Geophysics 58 (12), p. 1748 – 1763

Pratt, R.G., & Worthington, M.H. (1988) The application of diffraction tomography to cross-hole seismic data. Geophysics 53 (10), p. 1284 – 1294

Pratt, R.G. (1990) Inverse theory applied to multi-source cross-hole tomography. Part 2: Elastic wave equation method. Geophysical Prospecting 38, p. 311 – 329

Pratt., R.G. (1999) Seismic waveform inversion in the frequency domain, Part 1: Theory and verification in a physical scale model. Geophysics 64 (3), p. 888 – 901

Pratt, R. G., Hou, F., Bauer, K., Weber, M. (2005): Waveform tomography images of velocity and inelastic attenuation from the Mallik 2002 cross-hole seismic surveys. - In: Dallimore, S. R., Collett, T. S. (Eds.), Scientifique Results from Mallik 2002 Gas Hydrate Production Research Well Program,

Mackenzie Delta, Northwest Territories, Canada, (GSC Bulletin ; 585), Geological Survey of Canada, p. 14.

Reiter, D.T., & Rodi, W. (1996) Nonlinear waveform tomography applied to crosshole seismic data. Geophysics 61 (3), p. 902 - 913

Riedel, M. (2016) Efficient computation of seismic traveltimes in anisotropic media and the application in pre-stack depth migration. Dissertation at the TU Bergakademie Freiberg.

Ryberg, T., & Haberland, C. (2018) Bayesian inversion of refraction seismic traveltime data. Geophys. J. Int. 212, p. 1645–1656, doi: 10.1093/gji/ggx500

Ryberg, T., & Haberland, C. (2019): Bayesian simultaneous inversion for local earthquake hypocentres and 1-D velocity structure using minimum prior knowledge. - Geophysical Journal International, 218, 2, 840-854.doi: 10.1093/gji/ggz177

Sambridge, M. & Mosegaard, K. (2002) Monte Carlo methods in geophysical inverse problems, Rev. Geophys., 40 (3), 1009, doi:10.1029/2000RG000089

Shapiro N.M., Ritzwoller M.H. (2002) Monte-Carlo inversion for a global shear-velocity model of the crust and upper mantle, Geophys. J. Int., 151 (1), 88–105. 10.1046/j.1365-246X.2002.01742.x

Schott, J.-J., Roussignol, M., Menvielle, M., & Nomenjahanary, F.R. (1999) Bayesian inversion with Markov chains—II. The one-dimensional DC multilayer case, JGI 138 (3), pp 769–783, https://doi.org/10.1046/j.1365-246x.1999.00905.x

Sen, M.K., & Biswas, R. (2017) Transdimensional seismic inversion using the reversible jump Hamiltonian Monte Carlo algorithm. Geophysics 82 (3), p. R119 – R134.

Sethian, J. (1996) A fast marching level set method for monotonically advancing fronts. Proceedings of the National Academy of Sciences of the United States of America 93, 1591–1595.

Sethian, J.A. & Popovici, A. (1999) 3-D traveltime computation using the fast marching method, Geophysics , 64 , 516-523.

Takahashi, H., Fercho, E., & Dallimore, S.R. (2005) Drilling and operations overview of the Mallik 2002 Production Research Well Program; in Scientific Results from the Mallik 2002 Gas Hydrate Production Research Well Program, Mackenzie Delta, Northwest Territories, Canada, (ed.) S.R. Dallimore and T.S. Collett; Geological Survey of Canada, Bulletin 585, 14 p.

Titus, W.J., Titus, S.J., & Davis, J.R. (2017) A Bayesian approach to modeling 2D gravity data using polygons. Geophysics 82. G1 – G21. https://doi.org/10.1190/geo2016-0153.1

Thomsen, L. (1986) Weak elastic anisotropy. Geophysics 51, pp. 1954–1966.

Valcke, S. L. A. , Casey, M. , Lloyd, G. E. , Kendall, J.-M. , & Fisher, Q. J. (2006) Lattice preferred orientation and seismic anisotropy in sedimentary rocks, Geophysical Journal International, 166 (2), p. 652–666, doi: 10.1111/j.1365-246X.2006.02987.x

Wessel, P., Smith, W. (1998), New, improved version of the Generic Mapping Tool released, suppl. to EOS, Transactions, AGU, 79, 579.

Williamson, P.R., Sams, M.S., & Worthington, M.H. (1993) Crosshole imaging in anisotropic media. The Leading Edge January 1993, p. 19 – 23.

Figures:

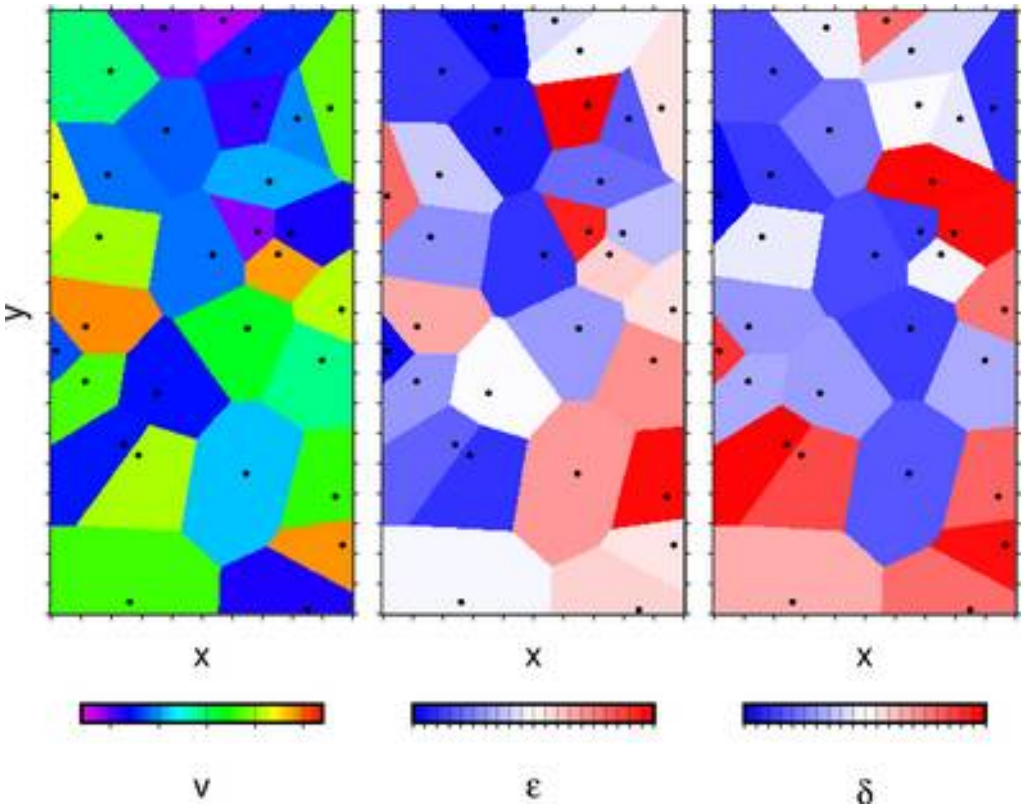

Figure 1: Schematic display of the model. The black dots represent the unstructured points p_i at spatial positions x_i and y_i to which v_i, ε_i and δ_i values are associated to. For the forward calculation three regular fine grids (for v, ε and δ) are used which are calculated from the Voronoi cells (points p_i).

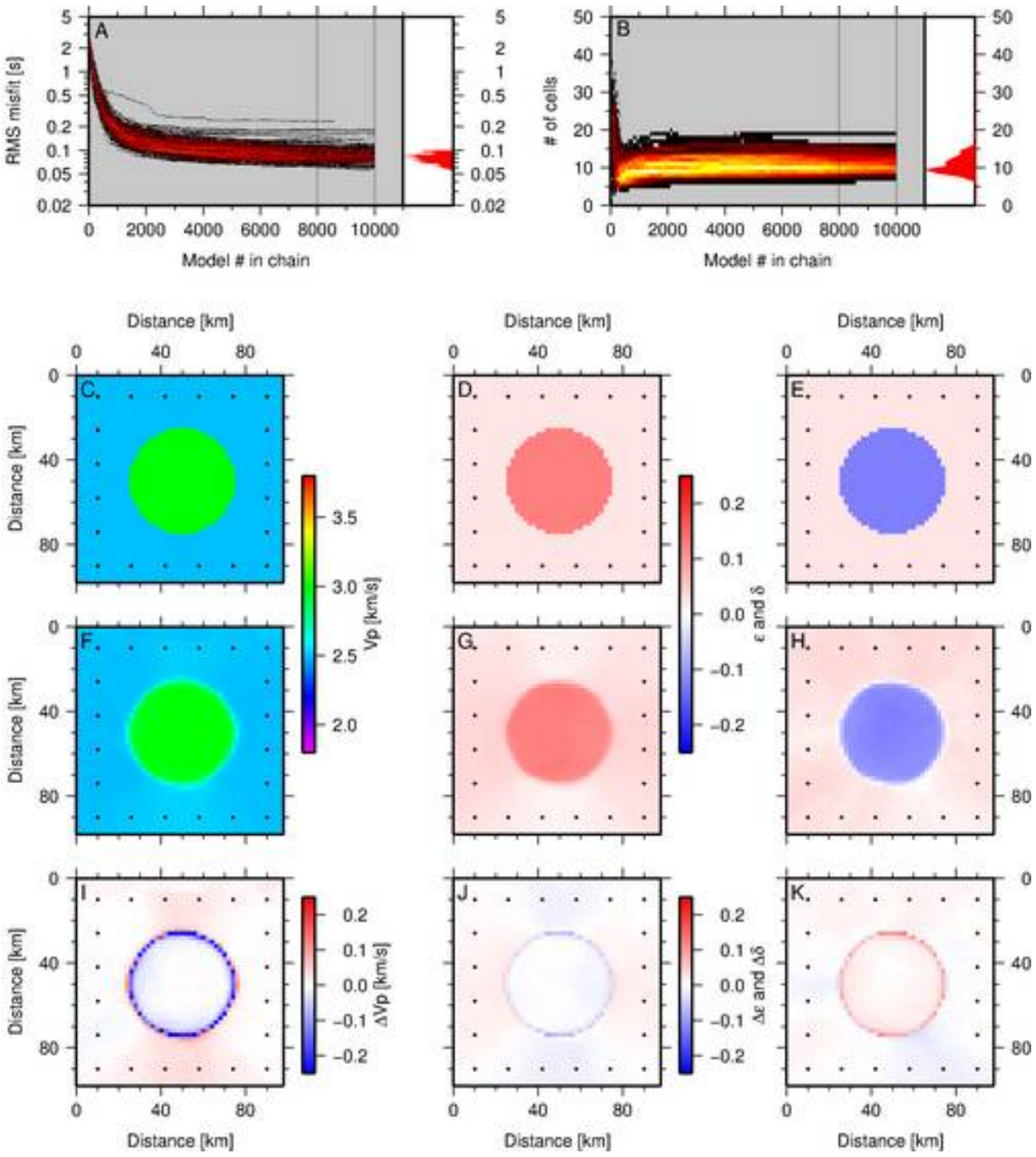

Figure 2: Recovery test of synthetic model with ideal source/receiver distribution. Evolution of misfit along Markov chains. Shown is the histogram distribution of the data misfit (A) and model dimension (number of cells, B) during the evolution along 200 Markov chains using a heat map color scale. The black line at 8000 shows the end of the burn-in phase, following models are used to derive the final model. Relative histogram plots of the distribution of data misfit (A) and model dimension (B) are added at the right sides, respectively. C, D and E show the synthetic models: v, ε and δ. Red/black dots show the location of the 20 sources & receivers (coinciding). F, G and H show the recovered models. The differences (F vs. C, etc.) are shown in I, J and K.

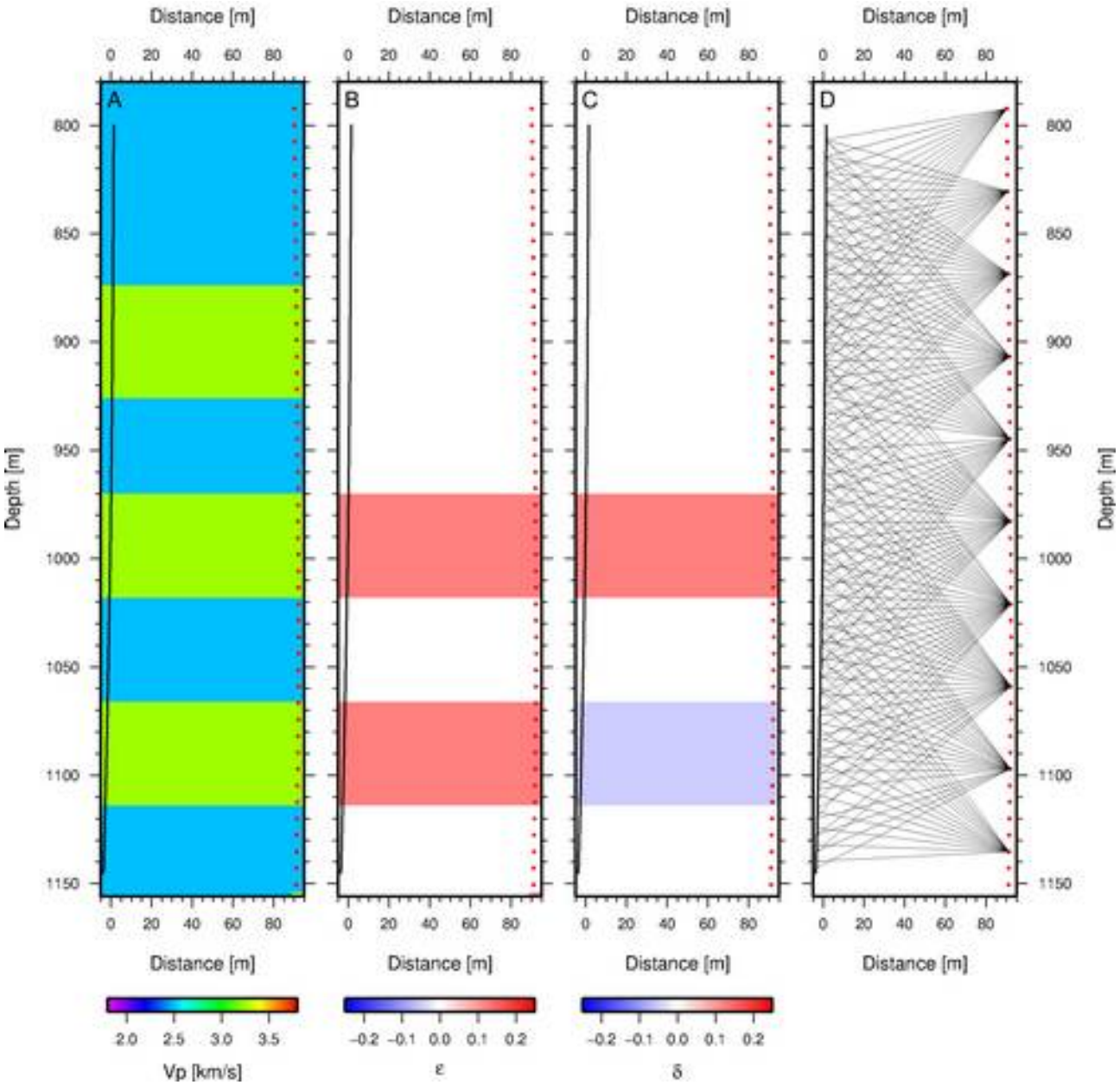

585 **Figure 3:** Recovery test of synthetic model with realistic source/receiver distribution for a cross-hole scenario with sources (red dots) and receivers (black dots) positioned on opposite sides of the model. A, B and C show the distribution of v, ε and δ of layered anomalies superimposed over a homogeneous background model. Red and black dots indicate the locations of sources and receivers, respectively. D shows a subset (decimated) of the ray coverage (for simplicity straight rays).

590

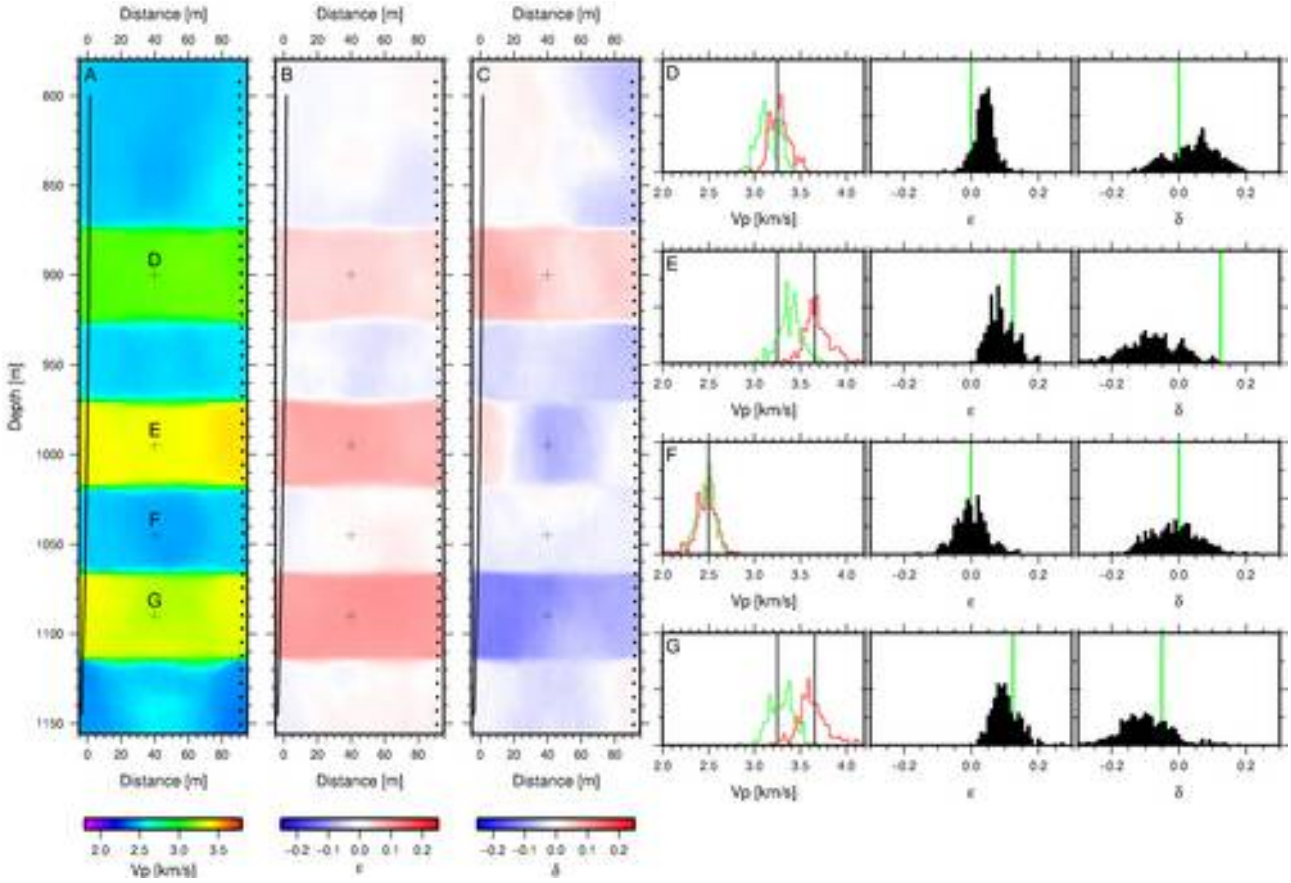

Figure 4: Recovery of the model from Fig. 2. A, B and C show the distribution of the recovered vertical velocity v, ε and δ parameters. Annotated crosses (D, E, F and G) show the locations where the posterior distribution of velocities (vertical green, horizontal red histograms), ε and δ (black histograms) are shown in the panels D, E, F and G. The black and green vertical lines in the histogram panels (D, E, F, G) show the input values for velocities, ε and δ, respectively. See text for more details.

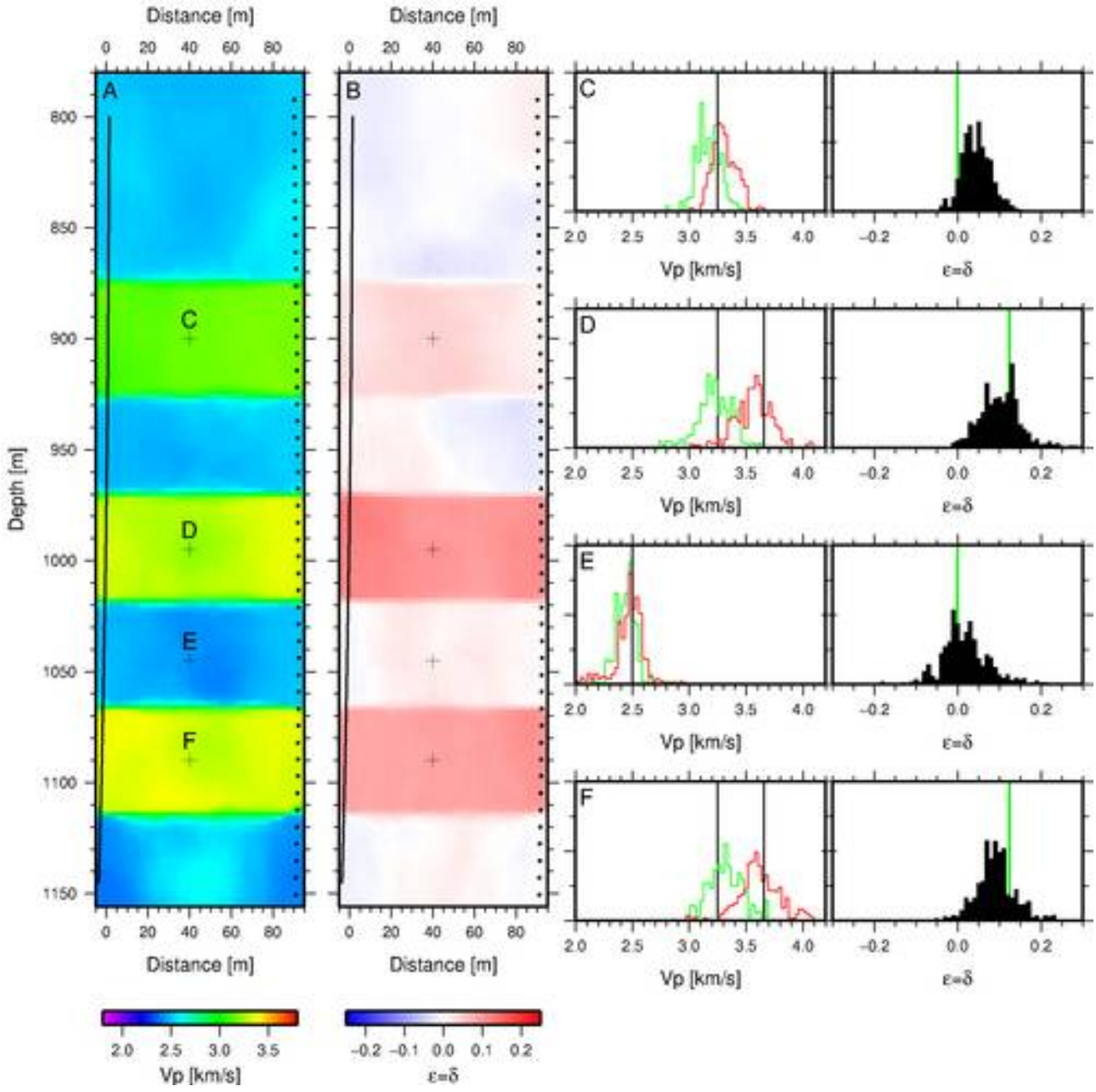

Figure 5: Recovery of the model from Fig. 2 but for the case ε=δ. A and B show the distribution of the recovered velocity and ε (=δ) parameter. Annotated crosses (C, D, E and F) show the locations where the posterior distribution of velocities (vertical green, horizontal red histograms) and ε (=δ) is shown in panels C, D, E and F. The black (green) lines in the left (right) set of histograms (panels C, D, E, F) show the input values for velocities and ε (=δ), respectively.

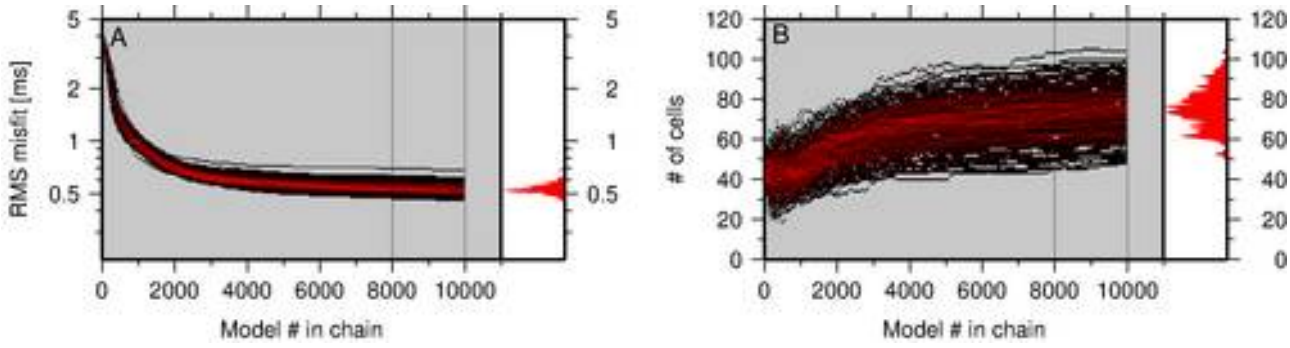

Figure 6: Evolution of misfit along Markov chains for the real data example for inversion of velocity and ε (=δ) assuming elliptical anisotropy. Shown is the histogram distribution of the data misfit (A) and model dimension (number of cells, B) during the evolution along 200 Markov chains using a heat map color scale. The black line at 8000 shows the end of the burn-in phase, following models are used to derive the final model. Relative histogram plots of the post burn-in distribution of data misfit (A) and model dimension (B) are added at the right sides, respectively.

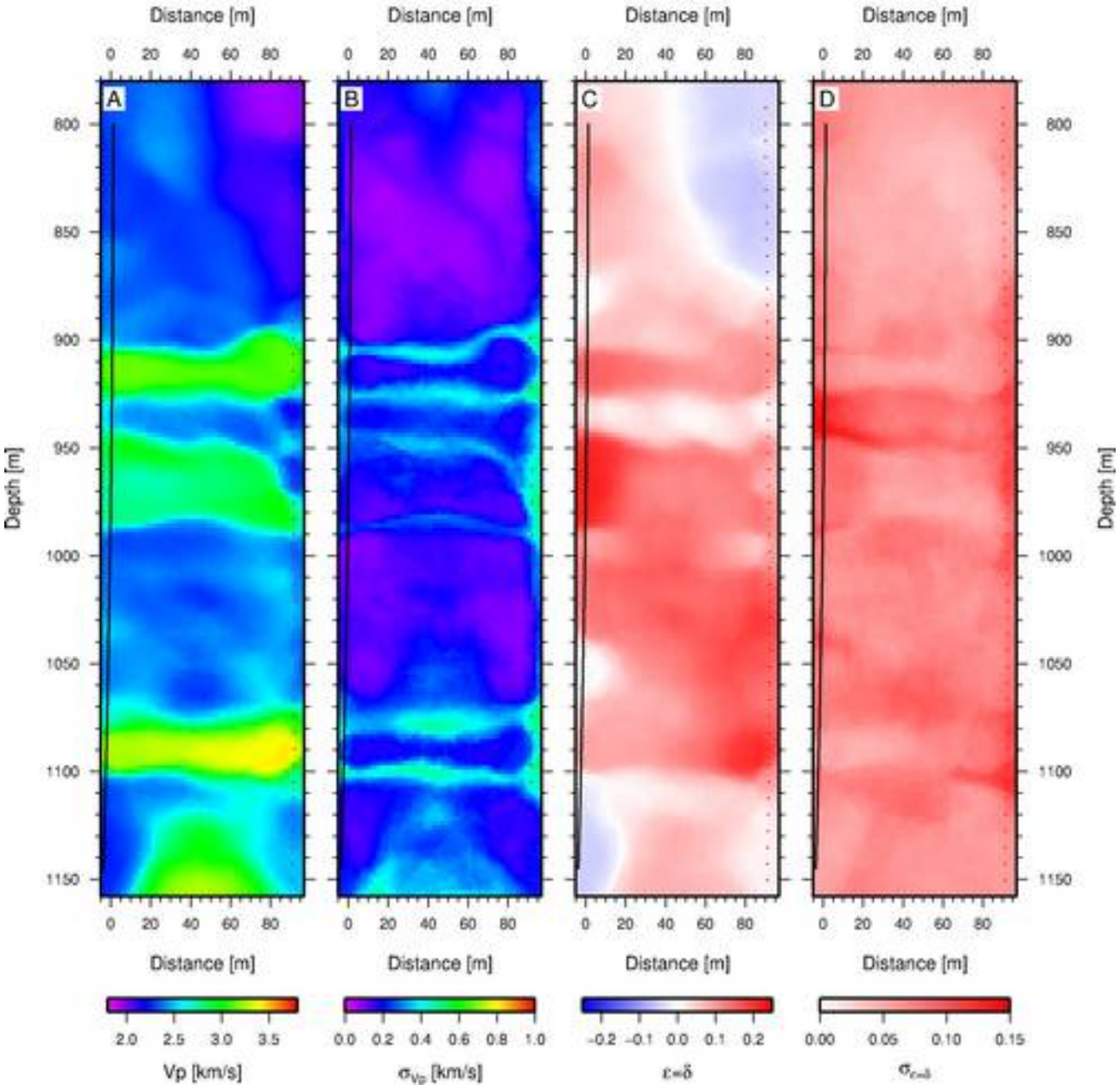

Figure 7: Results of the real data inversion: A shows the recovered velocity, B shows its uncertainty. At sharp velocity contrasts, the uncertainty is increased. C and D show the distribution of ε=δ and its uncertainty. The ε (=δ) model is dominated by positive (red) regions with less well-defined boundaries (no sharp increase of ε(=δ) uncertainty).

635

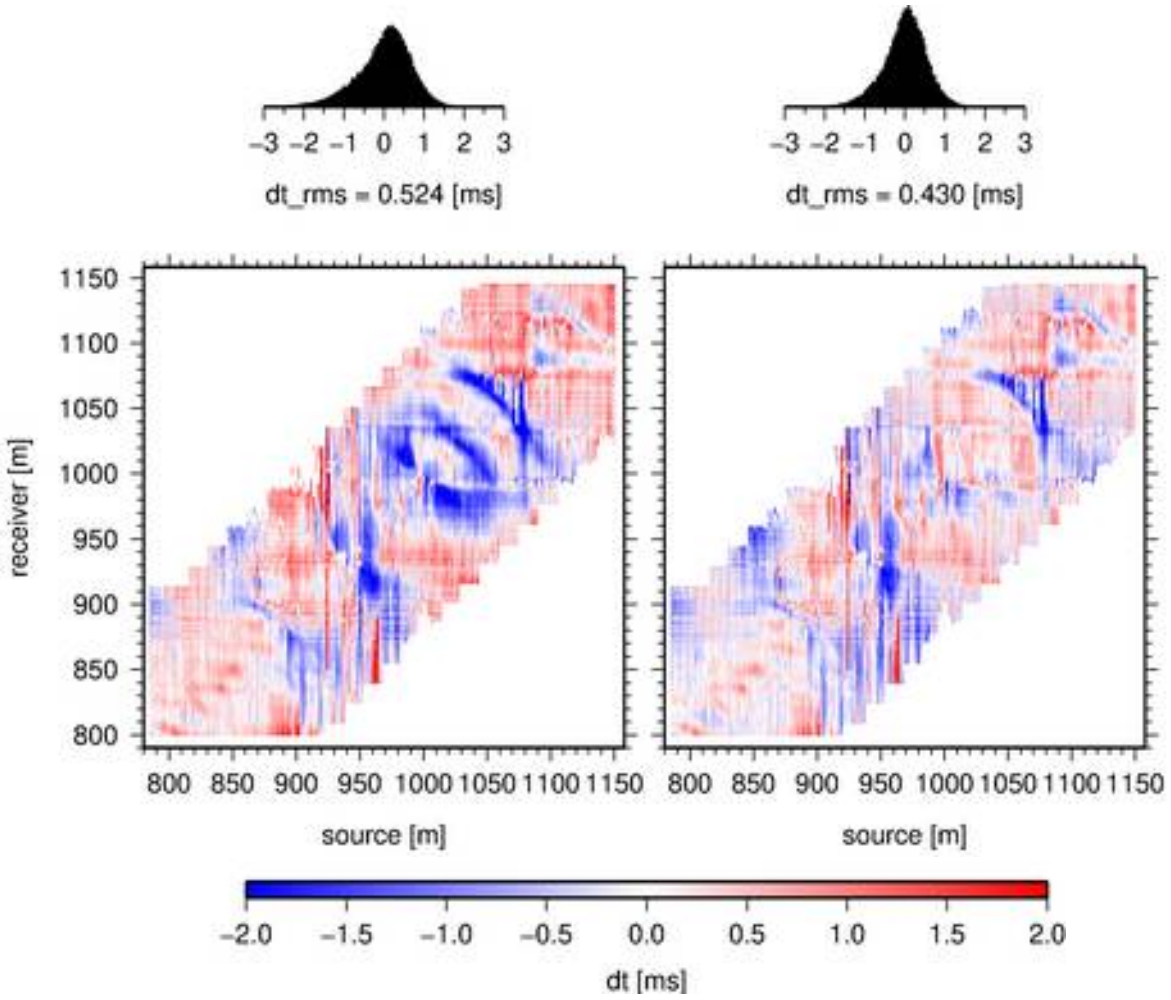

Figure 8: Distribution of traveltime residuals: left - isotropic inversion result, right – elliptical case, above RMS misfts

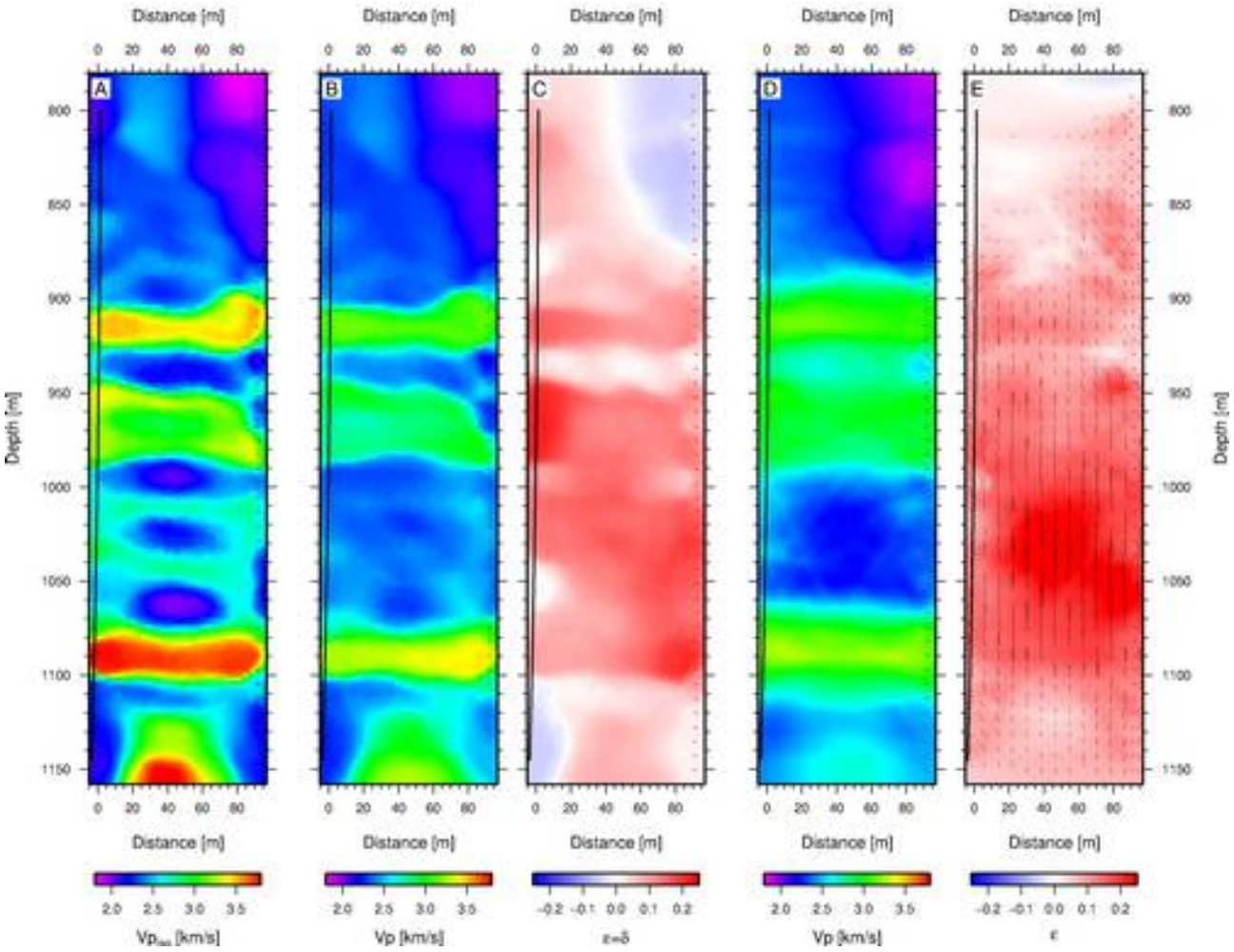

Figure 9: Comparison of models: A shows the velocity distribution assuming an isotropic wave propagation. This model is characterized by strong velocity contrast and has a relatively high data misfit (not shown). B and C show the vertical velocity and ε (=δ) distributions (see Fig. 6), with lower velocity contrasts and lower data misfit, compared to A. D and E are the inversion results from Bauer et al., 2006a,b (black lines in E represent the symmetry axis).